



HAL
open science

Capturing the pathomechanisms of different disease severities in a human cerebral organoid model of LIS1-lissencephaly

Andrea Carlo Rossetti, Olivia Fechtner, Camille Maillard, Anne Hoffrichter, Lea Zillich, Eric Poisel, Ammar Jabali, Fabio Marsoner, Ruven Wilkens, Fiona Francis, et al.

► **To cite this version:**

Andrea Carlo Rossetti, Olivia Fechtner, Camille Maillard, Anne Hoffrichter, Lea Zillich, et al.. Capturing the pathomechanisms of different disease severities in a human cerebral organoid model of LIS1-lissencephaly. *BioRxiv*, 2022, 10.1101/2022.12.19.520907 . hal-04301207

HAL Id: hal-04301207

<https://hal.science/hal-04301207>

Submitted on 23 Nov 2023

HAL is a multi-disciplinary open access archive for the deposit and dissemination of scientific research documents, whether they are published or not. The documents may come from teaching and research institutions in France or abroad, or from public or private research centers.

L'archive ouverte pluridisciplinaire **HAL**, est destinée au dépôt et à la diffusion de documents scientifiques de niveau recherche, publiés ou non, émanant des établissements d'enseignement et de recherche français ou étrangers, des laboratoires publics ou privés.

Capturing the pathomechanisms of different disease severities in a human cerebral organoid model of LIS1-lissencephaly

Andrea Carlo Rossetti^{1,2,3*}, Olivia Fechtner^{2,3,4*}, Camille Maillard⁵, Anne Hoffrichter^{1,2,3}, Lea Zillich⁶, Eric Poisel⁶, Ammar Jabali^{1,2,3}, Fabio Marsoner^{1,2,3}, Ruven Wilkens^{1,2,3}, Fiona Francis^{7,8,9}, Nadia Bahi-Buisson⁵, Philipp Koch^{1,2,3} and Julia Ladewig^{1,2,3,4§}

¹Department of Translational Brain Research, Central Institute of Mental Health (ZI), University of Heidelberg/Medical Faculty Mannheim, Germany. ²HITBR Hector Institute for Translational Brain Research gGmbH, Mannheim, Germany. ³German Cancer Research Center (DKFZ), Heidelberg, Germany. ⁴Institute of Reconstructive Neurobiology, University of Bonn School of Medicine & University Hospital Bonn, Bonn, Germany. ⁵Department of Pediatric Neurology, Université Paris Descartes, Imaging Institute, Paris, France. ⁶Department of Genetic Epidemiology in Psychiatry, Central Institute of Mental Health (ZI), University of Heidelberg/Medical Faculty Mannheim, Germany. ⁷INSERM UMR-S 1270, F-75005 Paris, France. ⁸Sorbonne University, F-75005 Paris, France. ⁹Institut du Fer à Moulin, F-75005 Paris, France.

* These authors equally contributed to this work.

§ Corresponding author

Correspondence: Julia.ladewig@zi-mannheim.de

Lissencephaly is a developmental cortical malformation characterized by reduced to absent gyri and a disorganized cortex. Heterozygous mutations in the LIS1 gene, encoding a regulator of the microtubule-motor dynein, were identified to cause lissencephaly with different severities. While the clinical disease spectrum correlates with the degree of lissencephaly, location and type of mutation does not. Here we present forebrain-type organoids from LIS1 patients with mild, moderate or severe lissencephaly that reflect disease severity in the degree of alterations of cytoarchitecture and neurogenesis. ScRNAseq data point toward a severity related dysregulation of progenitor cell homeostasis. Furthermore, we show that severity dependent alteration in microtubule stabilization is critical for the development of the phenotype. In addition, we found alterations in niche-dependent WNT-signaling mainly in severe patient-derived organoids. Thus, our data identify for the first time a clear association between the clinical severity grade of the patients and the molecular phenotype in the organoid model, suggest linked disease-mechanisms and show the sensitivity of organoid-based systems to capture different disease severities *in vitro*.

The human neocortex, critical for language, sociability, and sensorimotor control, is an expanded, highly organized and extensively folded (gyrencephalic) structure¹. Malformations of human cortical development are a vast and heterogeneous group of disorders with genetic or environmental aetiology and characterized by disruption of the cerebral cortex architecture². Heterozygous mutations in the LIS1 gene cause lissencephaly (smooth brain) in humans with diverse imaging and clinical phenotypes, ranging from mild pachygyria (broad gyri) to severe agyria (no gyri), resulting in epilepsy and intellectual disabilities¹. While the clinical severity generally correlates with the degree of lissencephaly, the location and type of mutation in the LIS1 gene does not³. From Lis1 mouse models we know that this protein regulates the microtubule motor cytoplasmic dynein, and through this function, dynein-dependent processes such as neuronal migration, interkinetic nuclear migration and mitotic spindle orientation⁴⁻⁹. Even though the observed phenotypes appeared, compared to humans, drastically milder in murine models -which are lissencephalic by nature- these studies suggested that LIS1 protein dosage is highly relevant for phenotypic severities^{10,11}. Nonetheless, (I) why specific human mutations in the LIS1 gene lead to the various degrees of severity in the patient and, (II) whether specific processes during cortical development are differentially affected by the different mutations, was so far not investigated. Here we explore the ability to investigate specific human LIS1

mutations and their association with the different disease severities of LIS1-lissencephaly using LIS1 patient-specific induced pluripotent stem (iPS) cells and derived forebrain-type cerebral organoids thereof.

From a cohort comprising 63 cases, we selected 7 LIS1 patients covering the whole spectrum of gyrification alterations of LIS1-lissencephaly, ranging from Dobyns grade 5 (mild) to 1 (severe)^{12,13}. Each patient harbors a molecularly characterized heterozygous mutation in the LIS1 gene (Extended Data 1A). Following reprogramming of patient-derived somatic cells to iPS cells, and their basic characterization (2 clones each, Extended Data 1B-I, Extended Data - Table 2), we validated the respective patient-specific LIS1 mutations by sequencing (Extended Data 1J-K). We then generated forebrain-type cerebral organoids¹⁴ from the 7 LIS1 patient and 7 control iPS cell lines. While organoids from control and patients with milder disease gradually developed regular neuroepithelial loop-like structures which expand over time, organoids from patients with moderate disease appeared to be generally smaller in size (Fig. 1A). Surprisingly, organoids from severe patients were not smaller compared to control derived organoids but developed irregular edges, with single cells noticeably growing away from the structures (Fig. 1A). Immunohistochemical analyses following whole-tissue clearing or cryo-sectioning showed that organoids derived from severe patients present a large belt of neurons which were less abundant in mild and moderate conditions and nearly absent in control-derived organoids (Fig. 1B, Extended Data 2A). When we further assessed the architecture of the individual neuroepithelial structures within the organoids by analyzing multiple ‘ventricular zone’ (termed VZ) dimension parameters, we found a significant reduction of all variables in organoids derived from patients with moderate and severe lissencephaly, as well as a significant reduction in 3 out of the 6 parameters analyzed in organoids from patients with mild lissencephaly compared to controls (Fig. 1C-D, Extended Data 2A). The decreased size of the VZ and the increase in the neuronal fraction - going from mild to moderate and severe- suggests a severity-dependent depletion of the progenitor pool in favor of an increase in neurogenesis. To further uncover the LIS1 severity-related changes, we performed single-cell RNA-sequencing (scRNA-seq) of organoids from 2 controls, 2 mild, 2 moderate and 2 severe patients (two to three pooled organoids at day 23±2 from two different genotypes per condition; Fig. 2A, Extended Data 3A). The different cell populations including neuroepithelial cells (NES), cycling progenitors (CyP), radial glia cells (RG), intermediate progenitors (IP), dorsal forebrain (dFB-N), ventral forebrain (vFB-N), midbrain (MB-N) and inter-neurons (IN), as well as glial cells (G), were identified based on known marker gene expression¹⁵⁻¹⁹ (Fig. 2B). When comparing the cell type composition, we

found a significant reduction in neural progenitor cells accompanied by a significant increase of neurons and glia in the LIS1 severe condition. This change in cell type composition was less abundant in mild and moderate conditions (Fig. 2C). When investigating the progenitor cell type composition (Fig 2D; Extended Data 3B) in more detail comparing control with mild, moderate and severe LIS1 patient-derived organoids, we found a depletion of NES cells in all patient samples (control: 20,9% \pm 2,2; mild: 0,04% \pm 0,1; moderate 0,46% \pm 0,5; severe 0,38% \pm 0,1). In addition, the mild and moderate patient organoids show an increase in RG (control 35,2% \pm 2,8; mild: 58,73% \pm 5,5; moderate: 49,57% \pm 1,3 (n.s), compared to the inverse trend for severe 10,77% \pm 2,2). As well as a decrease in RG, the samples from severe patients also show a possible decrease in CyP (control: 13,64% \pm 3,0; severe 7,14% \pm 1,0). In addition, the severe LIS1 patient-derived organoids present an independent progenitor cell cluster (perturbed progenitors, PP; control: 0,03% \pm 0,04; mild: 0,06% \pm 0,06; moderate: 0,22% \pm 0,18; severe: 26,01% \pm 0,80, Fig. 2A, D, Extended Data 3A-B) that, although expressing a similar marker profile compared to the RG cluster (Fig. 2B), shows a significant overrepresentation of GO terms connected to neuronal differentiation, including generation of neurons, neuronal fate commitment and regulation of neuron differentiation (Fig. 2E). Taken together, the scRNAseq data hint at a gradual impairment of progenitor homeostasis (even showing inverse trends in mild versus severe RG) and support the hypothesis that an accelerated neuronal differentiation phenotype is a key pathological phenomenon at least in severe cases.

We recently reported alterations of microtubule stability in the most severe form of lissencephaly, the Miller-Dieker Syndrome (MDS)²⁰. To assess whether the different patient-specific mutations have direct consequences on microtubule stability we performed immunostainings for acetylated (stable) alpha-tubulin (Ac-TUB) in whole-tissue cleared organoids and in individual VZ structures following cryo-sectioning. The cleared and stained organoids show a clear overall reduction of Ac-TUB positive labeled structures with increased disease severity when compared to control (Extended Data 4A). When investigating the individual VZ structures, we found that in control condition the span of Ac-TUB strands were aligned and in close proximity from the apical to the basal side, while in patient derived organoids the strand density was progressively decreased at the basal side with increased disease severity (Fig. 3A, B). Moreover, in parallel with the acetylated tubulin disruption, we observed an accumulative cellular disorganization of the VZ areas. Especially organoids derived from more moderate and severe cases displayed randomly arranged cell bodies with gaps in between the cells found in the VZ areas, whereas in control conditions these cells

were well organized (Fig. 3C). Besides, the apical membrane alignment (measured by the accumulation of N-cadherin) was disrupted in all patient organoids, most significantly in the moderate and severe conditions (Fig. 3D-E). To determine whether the destabilized microtubules in the patient-derived organoids directly shape the observed alterations in cytoarchitecture and / or neurogenesis, we applied the FDA approved drug Etoposide (a macrolide directly interacting with and stabilizing microtubules)²¹⁻²³ to LIS1 patient and control-derived organoids. Indeed, Etoposide treatment significantly increased the Ac-TUB strand density in basal VZ regions of LIS1 patient-derived samples (Fig. 3F, Extended Data 4B-C), significantly increased the diameter length in LIS1 severe VZ areas (Fig. 3G) and improved the generation of homogeneous and thick neuroepithelial VZ structures with improved apical membrane alignment (Extended Data Fig. 5A-B). In addition, the treatment resulted in a marked decrease of the neuronal belt surrounding the VZ structures with the most evident effect in organoids from patients with moderate and severe disease (Fig. 3H). Thus, although the treatment did not fully rescue the phenotype in patient-derived organoids, we show that microtubule destabilization is not only a shared mechanism with other forms of lissencephaly²⁰, but is also critical for the development of the phenotype with a severity dependent gradient.

We also recently found that alterations of the microtubule array and accompanied cellular disorganization of the VZ can lead to changes in niche-dependent WNT²⁰. We thus wondered whether WNT signaling might also be involved in the severity-related phenotype of our LIS1-patient derived organoids. To monitor the onset and localization of WNT-target gene activity in patient and control derived organoids, we generated WNT-GFP iPS cell reporter lines and differentiated them to forebrain-type organoids. We found that the apical lining of VZ structures from mild, moderate and severe LIS1-lissencephaly patients exhibit with increased disease severity a gradual decrease of WNT-target reporter activity signal compared to control (Fig. 4A, B). We further investigated expression of genes involved in WNT signaling in the CyP cluster -the cell population which most likely is associated with the progenitors at the apical lining- of the mild, moderate and severe condition compared to control. Here we found a significant downregulation of 23 out of 31 investigated genes connected to WNT signaling in the most severe condition while in the moderate condition only 4 and in the mild condition 3 of the WNT signaling genes were significantly downregulated (Fig. 4C). We further wondered whether the perturbed niche-dependent WNT-signaling results in a premature non-random switch of aRG cell division from progenitor cell expansion to neurogenesis as previously observed²⁰. Indeed, we found a clear increase in horizontal division patterns of

aRG cells in cultures derived from severe patients compared to controls. In addition, we observed an increase in oblique division modes (most likely a direct effect of the perturbed microtubule array) in all patient samples, which appeared the most prominent in patients with moderate disease (Fig. 4D). To further test to what extent perturbed WNT-signaling contributes to the observed patient-specific alterations we exposed control and patient-derived organoids to the GSK3 β inhibitor CHIR99021²⁴. Here we found that CHIR99021 treatment leads to a much more homogeneous generation of VZ structures, an increase in VZ diameter and a reduced neuronal belt surrounding the VZ area, most prominent in severe-patient derived organoids (Fig. 4E, F). In addition, the treatment rescues the switch in plane of cell division in organoids derived from severe patients while it does not significantly impact the plane of cell division in the control, mild and moderate condition (Fig. 4G). Thus, these data suggest that dysregulation of niche-dependent WNT-signaling strongly applies to the most severe form of LIS1-lissencephaly, but has no obvious effects in mild cases.

Taken together our data show that different patient-specific mutations in the LIS1 gene have a convergent cellular and molecular impact on the *in vitro* phenotype, based on the clinical diagnosis of the donor. By that, our study provides a strong connection between the patient-specific genetic background -including the respective mutation in the LIS1 gene- and the clinical severity grade and point towards a role of the different degrees of neuronal progenitor perturbation in the manifestation of the disease severity grades. This study also demonstrates the possibility to recapitulate different disease severities in cerebral organoids -a major challenge so far not addressed- and that the system is sensitive enough to model pathologies with a wide spectrum of phenotypes affecting early human cortical development.

Methods

Cell lines. Control skin fibroblasts were obtained from Coriell Biorepository (control 1, 2-years old female, catalog ID GM00969; control 2, 5-months old male donor, catalog ID GM08680). LIS1-patient fibroblasts and lymphocytes were collected and send from Nadja Bahi-Buisson from the Necker Enfants Malades university hospital in France (LIS1-mild 1, 8-years old male donor, c.569-10T>C LIS1 mutation; LIS1-mild 2, 5-years old male donor, c.569-10T>C LIS1 mutation; LIS1-moderate 1, 6-years old female donor, c.13del LIS1 mutation; LIS1-moderate 2, 13-years old female donor, delEx11 LIS1 mutation; LIS1-severe 1, 4-years old female donor, c.1002+1G>A; LIS1-severe 2, 18-years old female donor, c.531G>C LIS1-mutation; LIS1-severe 3, 3-years old female donor, c.445C>T LIS1

mutation). iPSC lines were generated with patient consent, and this study was ethically approved. In addition, 5 control iPS cell lines were received from Dr. Sandra Horschitz (Ethics Committee II of Medical Faculty Mannheim of Heidelberg University approval no. 2014-626N-MA, control 3, 21-years old female donor; control 4, 44-years old female donor; control 5, 25-years old female donor; control 6, 26-years old female donor, control 7, 23-years old male donor). A complete overview of the cell lines used in this study is provided in Extended Data - Table 1.

Reprogramming of fibroblasts and lymphocytes. Somatic cells were reprogrammed by non-integrative delivery of OCT4, SOX2, KLF4 and c-MYC using the CTSTM CytoTuneTM-iPS 2.1 Sendai Reprogramming Kit (Thermo Fisher). The manufacturer's instructions were strictly followed (CTSTM CytoTuneTM-iPS 2.1 Sendai Reprogramming Kit User Guide).

iPS cell cultures maintenance. iPS cells were maintained on Geltrex-coated cell culture plates (Thermo Fisher) in Pluripro (PP) medium (Cell guidance systems) or Essential 8 (E8) medium at 37 °C, 5% CO₂ and ambient oxygen level with daily medium change. For passaging cells were with TrypLE Express (Stem Cell Technologies) or EDTA (Thermo Fischer Scientific). After passaging, medium was supplemented with 5µM Y-27632 (CellGuidance Systems) to foster cell survival. All human iPS cell lines were regularly tested and confirmed negative for mycoplasma.

Generation of WNT-GFP reporter iPS cell lines. iPS cells were transduced with a Lentivirus expressing GFP under activation of WNT signaling (Lentiviral-Top-dGFP reporter, Addgene plasmid #14715). Puromycin (1µg/ml, Sigma-Aldrich) selection was initiated 48 h following transduction. iPS cells-WNT reporter lines were used for cortical organoid generation.

Generation of 3D cortical forebrain-type organoids. Cerebral forebrain-type organoids were generated as previously described^{14,19}. Organoids were kept in 10cm or 6cm dishes under agitation at 70rpm on an orbital shaker (Infors Celltron HD) at 37°C, 5% CO₂ and ambient oxygen level. Media was changed every 3 to 4 days. Organoids were harvested for phenotypical analysis at day 15 and 20; for scRNA-seq at day 20±3. For immunostaining, 20µm sections of organoids were prepared using a cryotome. At least 6 organoids for each of three different batches were analyzed for all analysis. The given n number is the total of VZ structures analyzed, which always includes at least 3 biological replicates.

CHIR99021 and EpoD Treatment. Organoids were treated after the induction phase, from culture day 10 to day 15. The drugs were respectively resuspended in DMSO to reach the

concentration of 1 μ M CHIR or 1nM EpoD respectively. After treatment, organoids were fixed and cryo-sectioned for immunocytochemical analysis.

Histology and Immunocytochemistry. Cells and organoids were fixed with 4% paraformaldehyde (PFA) for 10 min at room temperature (RT) and blocked with 0,1% Triton and 10% FCS for 1h at RT. Primary antibodies were diluted according to the manufacturer's instructions and incubated over night at 4°C (Ac-TUB (1:500, Cell signaling), AFP (1:200, Hölzel), TUBB3 (1:2000, Cell Signaling), NANOG (1:200, DSHB), N-CAD (1:500, BD), p-VIM (1:500, Novus biologicals), TPX2 (1:500, Novus Biologicals), OCT3/4 (1:500, R&D Systems), SMA (1:400, Abcam), SSEA3 (1:500, Santa Cruz) and SOX2 (1:500, Santa Cruz)). The secondary antibodies were diluted according to the manufacturer's instructions and incubated for 1h at RT (488-ms/rb; 555-ms/rt; 647-ms, 1:1000, Invitrogen). Nuclei were visualized using 0,1 μ g/ml DAPI (Sigma Aldrich). The HE staining was done with hematoxylin solution (Carl Roth) for 10min and 0,5% eosin solution (Carl Roth) for 5 min. For dehydration and clearing 70%, 80%, 90% and 100% ethanol solution was used. Stained sections were stored at 4°C and imaged using the Inverted Leica DMIL LED Microscope with the Thunder imaging software (Leica).

Clearing of 3D cortical forebrain-type organoids. For whole tissue mounting organoids were fixed with 4% PFA for 2 h at RT and optical cleared according to Susaki et al.²⁵. Blocking was done with 10% horse serum, 0.2% gelatin from cold water fish skin and 0.1% Triton X-100 diluted in PBS for 24 h at 37°C, followed by primary antibody incubation for 48 h at 37°C. Secondary antibody incubation was done for 48 h at 37°C. Refractive index matching was performed according to Nürnberg et al.²⁶ by immersion of samples in an aqueous solution of glycerol (RI=1.457) for 48 h at RT. Samples were mounted in U-shaped 2.5mm glass capillaries by embedding in 0.1% low melting agarose in ddH₂O. For light sheet microscopy, glass capillaries were transferred into 35mm glass bottom dishes, immobilized by agarose embedding and immersed in RI-matched glycerol solution. For temperature adjustment, samples were kept in the microscopy room for at least 24 h prior to image acquisition. Image acquisition was done using a Leica Microsystems TCS SP8 DLS, equipped with LAS X software, L 1.6x/0.05 DLS illumination objective, HC APO L 10x/0.30 W DLS detection objective and 7.8mm Glycerol DLS TwinFlect mirrors. Image stacks were acquired with a step size of 3.7 μ m and fused with LAS X.

Cortical organoids dissociation for single cell RNA-sequencing. 20 +/- 3-day organoids (3 or 2 per condition: control C1, control C7, LIS1-mild P1, LIS1-mild P2, LIS1-moderate P3,

LIS1-moderate P4 and LIS1 severe P5, LIS1-severe P6) were cut with a scalpel and dissociated according to our already published protocol¹⁹. Briefly, the tissue was incubated in papain (Sigma Aldrich) containing buffer (1 mM L-cysteine and 0,5mM EDTA in Earle's balanced salt solution, 20 units of papain, and 10µg/ml of DNase (Sigma Aldrich)) for 20 min at 37°C. After incubation, organoids were washed with differentiation media and dissociated mechanically using a 1% bovine serum albumin (BSA)-coated 1000µl pipette. After centrifugation at 400 g for 4 min at 4°C, the cell pellet was resuspended in 1 ml ice-cold PBS supplemented with 0.04% BSA and filtered through a 30 µm cell strainer. Single cell library preparation was performed using the 10x Genomics Chromium platform according to the 10x Genomics Chromium Single Cell 3' Library & Gel Bead Kit v3.1 chemistry user guide (10x Genomics). The prepared cDNA libraries were processed by the High Throughput Sequencing Unit of the Genomics & Proteomics Core Facility of the German Cancer Research Centre (DKFZ). The libraries were sequenced on 2 lanes of the Illumina NovaSeq 6k platform on a S1 flow cell (paired-end 28+94 bp).

Organoid quantifications. Organoid quantification were performed as previously described²⁰ with slight adaptations. Images were acquired using the Inverted Leica DMIL LED Microscope with the Thunder imaging software (Leica) and analyzed using ImageJ software. All quantifications were done in at least 3 organoids with at least 6 VZ structures for each of at least 3 different organoid batches. For the quantification of the VZ dimension parameters sections were stained with DAPI. Length and area measurements were performed with Image J software. For the VZ diameter 3 measurements for each cortical VZ structure were performed forming a right-angle fan area pointing to the nearest pial surface at 0, 45 and 90 degrees. The mean of all 3 values was taken as VZ diameter. In case of heterogenous VZ thickness, the thickest area was considered. The VZ tissue area was defined as the ratio of the total VZ area to the ventricle area. AC-TUB strand density was measured by plot profile determination using ImageJ software and a self-designed excel file containing formulas for background subtraction and automatic signal peak counting. The disruption diameter of N-CAD was measured at 4 apical membrane positions (90, 180, 270 and 360 degree) using ImageJ software. The mean value was taken as disruption diameter. Mitotic spindles were analyzed by immunocytochemical staining's using p-VIM for marking dividing aRG cells at the apical membrane and TPX2 for the visualization of mitotic spindle.

ScRNA-seq data quality control and preprocessing. Count matrices for single-cell RNAseq data were generated from fastq files using cellranger (10x Genomics). Data analysis was performed using Seurat v.4.0.5²⁷, if not stated otherwise. During quality control, features that

were not expressed in any cell were removed from the count matrix. Next, cells were removed in each replicate individually based on the number of expressed features, total UMI counts, and mitochondrial gene fraction (>10%). For detailed QC parameters, see Extended Data - Table 18. For each sample, normalization was performed using *sctransform*. Cell cycle differences (S.Score-G2M.Score) were regressed out and cell multiplets were removed using the R package DoubletFinder v.2.0.3²⁸. Integration of data was performed in two steps: first, for every condition, the two samples were integrated, followed by an integration of the four integrated objects resulting in the final Seurat object. UMAP dimensionality reduction and nearest-neighbor graph construction were performed based on dims 1:50. A resolution threshold of 0.15 was used for cluster generation. Cluster identity was determined based on the expression of known cell type markers. The intermediate progenitor (IP) cluster was manually split into two clusters according to normalized expression levels of the EOMES gene (>0.25) yielding a total of 10 clusters in the final object.

Differential expression testing. A threshold of 0.25 was set as the minimum percentage for gene expression in clusters. Differential gene expression between clusters was tested using *FindMarkers()*. To further investigate expression signatures in progenitor clusters of the Severe condition, *FindAllMarkers()* was applied to identify genes that separate the clusters from each other. A heatmap was generated displaying the 250 genes with the strongest log₂FC between clusters.

Pathway enrichment analysis. Enrichment analysis of cellular pathways (GO and HALLMARK) within specific clusters was performed based on the proportion of normalized counts related to a specific pathway. For this, genes contributing to a GO term/HALLMARK pathway were retrieved using the *org.Hs.eg.db* package (v.3.14.0). The number of counts attributed to the pathway genes was calculated and divided by the total number of counts resulting in a proportion estimate for every cell. Using a Wilcoxon rank-sum test, the statistical significance of enrichment in clusters was tested. Bonferroni correction was used to adjust for multiple testing if multiple conditions were compared.

Data and code availability. Any information required to reanalyze the data reported in this study is available from the lead contact upon request.

General statistical analysis. Quantitative data was generated in at least triplicates and tested for gaussian distribution using the Kolmogorov-Smirnov-Test. The Levene-test was applied to test for homogeneity of variances. If the data was characterized by gaussian distribution

one-way-Anova was used to determine significance. If one of the test assumptions were hurt, the significance was determined using Kruskal-Wallis- and Post-Hoc-Test (for details see Extended Data - Table 3-17).

Acknowledgements

We thank Isabell Moskal, Helene Schamber and Elina Nürnberg for the pivotal technical support. We thank the DKFZ SIngle-Cell Open Lab (scOpenLab) for assistance with the scRNA sequencing experiment. We acknowledge the support of the NGS Core Facility Mannheim, Medical Faculty Mannheim of Heidelberg University. The work was supported by the Ministry of Innovation Science and Research of North Rhine-Westphalia (Junior Research Group, to J.L.), the ERA-NET NEURON, JTC 2015 Neurodevelopmental Disorders, STEM-MCD (to J.L., F.F. and N.B-B) and the generous financial support by the Hector Stiftung II (to JL).

Author Contribution

Conceptualization, A.C.R., O.F., P.K., F.F., and J.L.; Methodology, A.C.R., O.F., S.H., A.J., F.M., R.W. and J.L.; Validation, A.C.R., O.F.; Formal Analysis, O.F.; Investigation, A.C.R., O.F.; ScRNA-Seq Data analysis, A.H., L.Z., E.P, A.C.R.; Whole-exome-sequencing, C.M. and N.B-B; Writing – Original Draft, O.F.; Writing – Reviewing & Editing, A.C.R., P.K. F.F. and J.L.; Visualization, A.C.R., O.F.; Supervision, J.L.; Project Administration, J.L.; Funding Acquisition, N.B-B, F.F., J.L.

Competing Interest

The authors declare no competing interests.

References

1. Florio M, Huttner WB. Neural progenitors, neurogenesis and the evolution of the neocortex. *Development*. Jun 2014;141(11):2182-94. doi:10.1242/dev.090571
2. Severino M, Geraldo AF, Utz N, et al. Definitions and classification of malformations of cortical development: practical guidelines. *Brain*. 10 01 2020;143(10):2874-2894. doi:10.1093/brain/awaa174
3. Saillour Y, Carion N, Quelin C, et al. LIS1-related isolated lissencephaly: spectrum of mutations and relationships with malformation severity. *Arch Neurol*. Aug 2009;66(8):1007-15. doi:10.1001/archneurol.2009.149

4. Faulkner NE, Dujardin DL, Tai CY, et al. A role for the lissencephaly gene LIS1 in mitosis and cytoplasmic dynein function. *Nat Cell Biol.* Nov 2000;2(11):784-91. doi:10.1038/35041020
5. Smith DS, Niethammer M, Ayala R, et al. Regulation of cytoplasmic dynein behaviour and microtubule organization by mammalian Lis1. *Nat Cell Biol.* Nov 2000;2(11):767-75. doi:10.1038/35041000
6. Yingling J, Youn YH, Darling D, et al. Neuroepithelial stem cell proliferation requires LIS1 for precise spindle orientation and symmetric division. *Cell.* Feb 08 2008;132(3):474-86. doi:10.1016/j.cell.2008.01.026
7. Moon HM, Youn YH, Pemble H, Yingling J, Wittmann T, Wynshaw-Boris A. LIS1 controls mitosis and mitotic spindle organization via the LIS1-NDEL1-dynein complex. *Hum Mol Genet.* Jan 15 2014;23(2):449-66. doi:10.1093/hmg/ddt436
8. Pawlisz AS, Mutch C, Wynshaw-Boris A, Chenn A, Walsh CA, Feng Y. Lis1-Nde1-dependent neuronal fate control determines cerebral cortical size and lamination. *Hum Mol Genet.* Aug 15 2008;17(16):2441-55. doi:10.1093/hmg/ddn144
9. Tsai JW, Chen Y, Kriegstein AR, Vallee RB. LIS1 RNA interference blocks neural stem cell division, morphogenesis, and motility at multiple stages. *J Cell Biol.* Sep 12 2005;170(6):935-45. doi:10.1083/jcb.200505166
10. Youn YH, Pramparo T, Hirotsune S, Wynshaw-Boris A. Distinct dose-dependent cortical neuronal migration and neurite extension defects in Lis1 and Ndel1 mutant mice. *J Neurosci.* Dec 09 2009;29(49):15520-30. doi:10.1523/JNEUROSCI.4630-09.2009
11. Gambello MJ, Darling DL, Yingling J, Tanaka T, Gleeson JG, Wynshaw-Boris A. Multiple dose-dependent effects of Lis1 on cerebral cortical development. *J Neurosci.* Mar 01 2003;23(5):1719-29.
12. Barkovich AJ, Guerrini R, Kuzniecky RI, Jackson GD, Dobyns WB. A developmental and genetic classification for malformations of cortical development: update 2012. *Brain.* May 2012;135(Pt 5):1348-69. doi:10.1093/brain/aws019
13. Barkovich AJ, Kuzniecky RI, Jackson GD, Guerrini R, Dobyns WB. A developmental and genetic classification for malformations of cortical development. *Neurology.* Dec 27 2005;65(12):1873-87. doi:10.1212/01.wnl.0000183747.05269.2d
14. Krefft O, Jabali A, Iefremova V, Koch P, Ladewig J. Generation of Standardized and Reproducible Forebrain-type Cerebral Organoids from Human Induced Pluripotent Stem Cells. *J Vis Exp.* 01 23 2018;(131)doi:10.3791/56768

15. Pollen AA, Nowakowski TJ, Chen J, et al. Molecular identity of human outer radial glia during cortical development. *Cell*. Sep 24 2015;163(1):55-67. doi:10.1016/j.cell.2015.09.004
16. Nowakowski TJ, Bhaduri A, Pollen AA, et al. Spatiotemporal gene expression trajectories reveal developmental hierarchies of the human cortex. *Science*. 12 08 2017;358(6368):1318-1323. doi:10.1126/science.aap8809
17. Liu J, Liu W, Yang L, et al. The Primate-Specific Gene TMEM14B Marks Outer Radial Glia Cells and Promotes Cortical Expansion and Folding. *Cell Stem Cell*. Nov 02 2017;21(5):635-649.e8. doi:10.1016/j.stem.2017.08.013
18. Velasco S, Kedaigle AJ, Simmons SK, et al. Individual brain organoids reproducibly form cell diversity of the human cerebral cortex. *Nature*. 06 2019;570(7762):523-527. doi:10.1038/s41586-019-1289-x
19. Jabali A, Hoffrichter A, Uzquiano A, et al. Human cerebral organoids reveal progenitor pathology in EML1-linked cortical malformation. *EMBO Rep*. 05 04 2022;23(5):e54027. doi:10.15252/embr.202154027
20. Iefremova V, Manikakis G, Krefft O, et al. An Organoid-Based Model of Cortical Development Identifies Non-Cell-Autonomous Defects in Wnt Signaling Contributing to Miller-Dieker Syndrome. *Cell Rep*. 04 2017;19(1):50-59. doi:10.1016/j.celrep.2017.03.047
21. Giannakakou P, Gussio R, Nogales E, et al. A common pharmacophore for epothilone and taxanes: molecular basis for drug resistance conferred by tubulin mutations in human cancer cells. *Proc Natl Acad Sci U S A*. Mar 14 2000;97(6):2904-9. doi:10.1073/pnas.040546297
22. Fumoleau P, Coudert B, Isambert N, Ferrant E. Novel tubulin-targeting agents: anticancer activity and pharmacologic profile of epothilones and related analogues. *Ann Oncol*. Jul 2007;18 Suppl 5:v9-15. doi:10.1093/annonc/mdm173
23. Bollag DM, McQueney PA, Zhu J, et al. Epothilones, a new class of microtubule-stabilizing agents with a taxol-like mechanism of action. *Cancer Res*. Jun 01 1995;55(11):2325-33.
24. Pachenari N, Kiani S, Javan M. Inhibition of glycogen synthase kinase 3 increased subventricular zone stem cells proliferation. *Biomed Pharmacother*. Sep 2017;93:1074-1082. doi:10.1016/j.biopha.2017.07.043
25. Susaki EA, Tainaka K, Perrin D, et al. Whole-brain imaging with single-cell resolution using chemical cocktails and computational analysis. *Cell*. Apr 24 2014;157(3):726-39. doi:10.1016/j.cell.2014.03.042

26. Nürnberg E, Vitacolonna M, Klicks J, et al. Routine Optical Clearing of 3D-Cell Cultures: Simplicity Forward. *Front Mol Biosci.* 2020;7:20. doi:10.3389/fmolb.2020.00020
27. Hao Y, Hao S, Andersen-Nissen E, et al. Integrated analysis of multimodal single-cell data. *Cell.* 06 24 2021;184(13):3573-3587.e29. doi:10.1016/j.cell.2021.04.048
28. McGinnis CS, Murrow LM, Gartner ZJ. DoubletFinder: Doublet Detection in Single-Cell RNA Sequencing Data Using Artificial Nearest Neighbors. *Cell Syst.* 04 24 2019;8(4):329-337.e4. doi:10.1016/j.cels.2019.03.003

Figure captions

Figure 1: Organoid morphology mimics LIS1 patient severity. (A) Representative brightfield images of control C1.2, mild P1.1, moderate P3.1 and severe P5.1 LIS1 patient-derived organoids at day 20. (B) Representative light sheet microscopy (LSM) pictures of whole-tissue cleared control C2.1, mild P1.1, moderate P3.2 and severe P5.1 patient-derived organoids at day 20, stained for β -III Tubulin (TUBB3). (C) Representative DAPI pictures of ventricular zone structures (VZ) of control C1.2, mild P1.1, moderate P3.1 and severe P5.1 patient-derived organoids at day 20. Yellow dotted lines define the VZ areas. (D) Quantification of VZ diameter, length of apical membrane, total VZ area, ventricle-like area, length of basal membrane and VZ tissue area in control (C1.2, C4.2) and LIS1 (P1.1, P1.2, P2.1, P2.2, P3.1, P3.2, P4.1, P4.2, P5.1, P5.2, P6.1, P6.2, P7.1) patient-derived organoids at day 20. (Control N=71, mild N=81, moderate N=77, severe N=240, total N=469). Scale bars, (A, B) 200 μ m (C) 50 μ m. Error bars, \pm SD. *P< 0.05, **P< 0.01, ***P< 0.001.

Figure 2: ScRNA-seq identifies a gradual increase in neurogenesis and impaired progenitor cell homeostasis with increased LIS1 severity. (A) Schematic representation of the scRNAseq experiment. UMAP dimensional reduction and unbiased clustering reveals 10 distinct color-coded cell populations within control, mild-, moderate- and severe LIS1 patient-derived organoids. Number of organoids and cells analyzed: 23 organoids, day 23 \pm 2, C1 N=3, 3265 cells; C7 N=3, 4988 cells; P1 N=3, 896 cells; P2 N=3, 2548 cells; P3 N=2, 2804 cells; P4 N=3, 2364 cells; P5 N=3, 3837 cells; P6 N=2, 3886 cells. (B) Dot plot graph showing the expression of markers used to identify the different cellular populations (neuroepithelial cells (NES), cycling progenitors (CyP), radial glia cells (RG), intermediate progenitors (IP), perturbed progenitors (PP), dorsal forebrain (dFB-N), ventral forebrain (vFB-N), midbrain (MB-N), interneurons (IN) and glial cells (G)). (C) Quantification of the percentage of neural progenitors (NES, CyP, RG, IP, PP) versus neurons and glial cells (dFB-N, vFB-N, MB-N, IN, G) in control, mild, moderate and severe derived samples. (D) Quantification of the percentage of NES, CyP, RG, IP and PP in control, mild, moderate and severe. (E) Violin plot showing the percentage of counts in RG and PP belonging to the set of genes associated with the GO terms neuronal differentiation, generation of neurons, neural fate commitment and regulation of neuron differentiation. Error bars, \pm SD. *P< 0.05, **P< 0.01, ***P< 0.001.

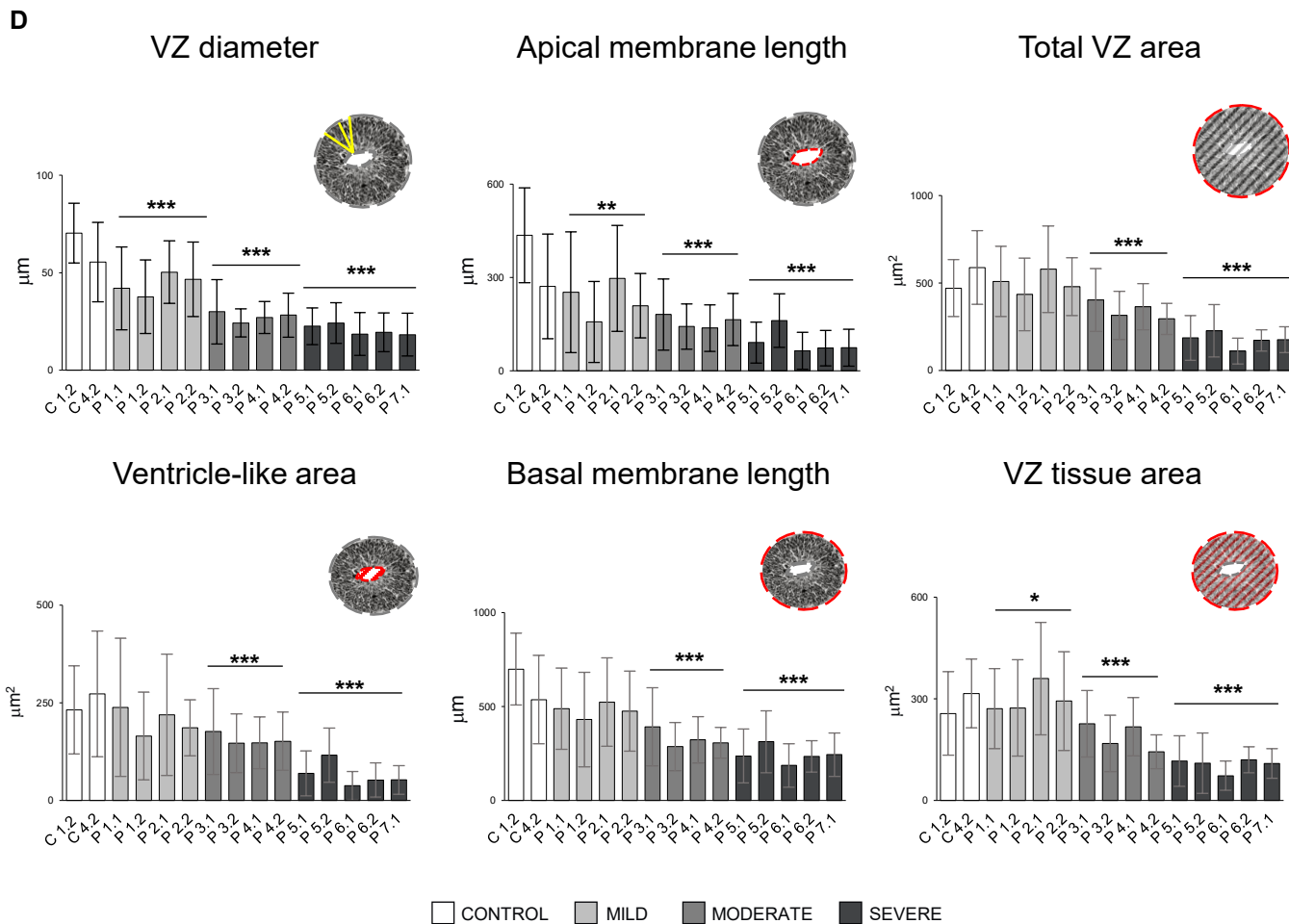
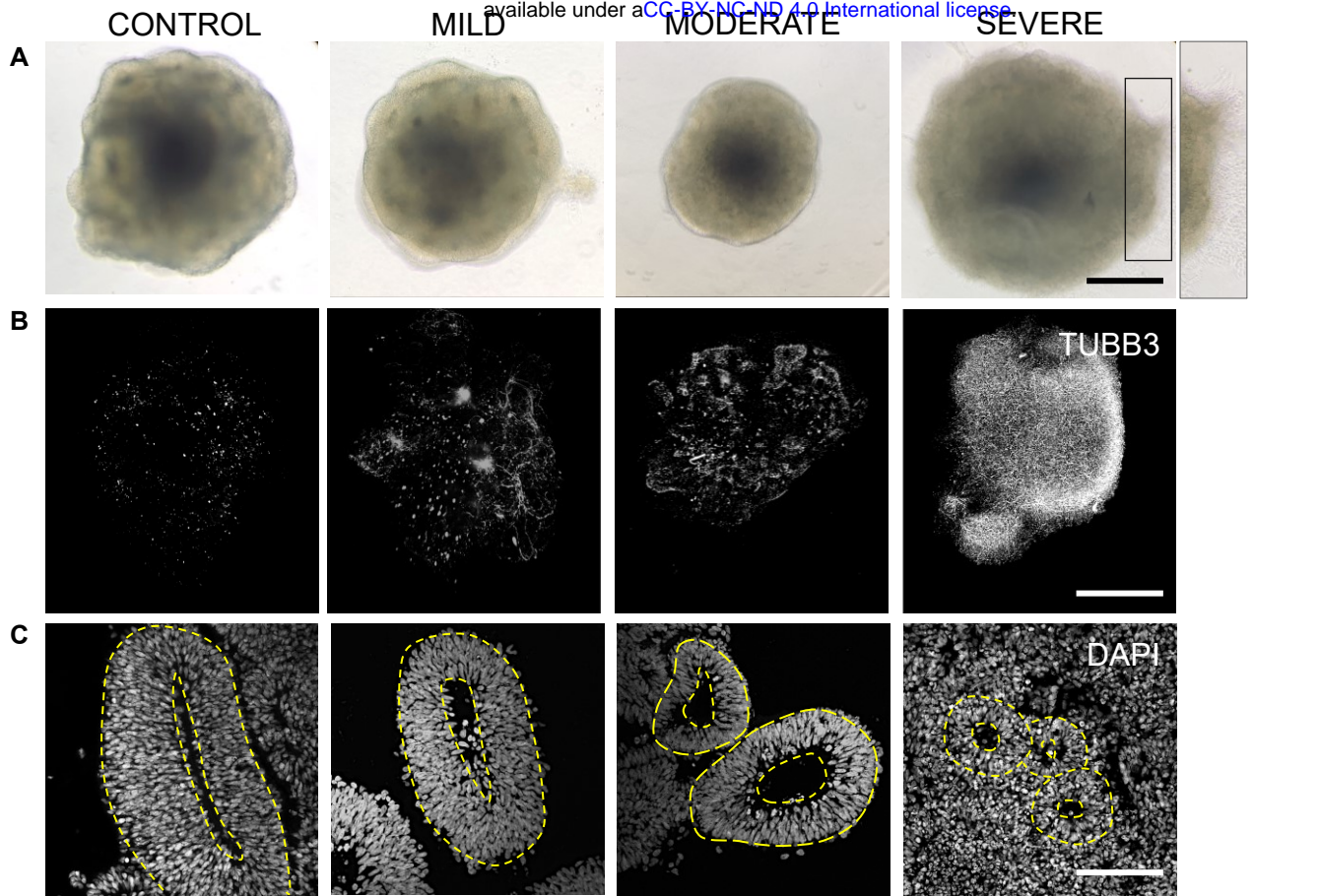
Figure 3: Severity dependent cytoarchitectural breakdown can be partially restored by microtubule array stabilization. (A) Representative images of control C4.1, mild P1.1, moderate P3.2 and severe P5.2 LIS1 patient-derived organoids stained for acetylated α -

tubulin (Ac-TUB) at day 20. **(B)** Quantification of apical and basal Ac-TUB strand density in control, mild, moderate and severe LIS1 patient-derived organoids at day 20, control N=20, mild N=59, moderate N=50, severe N= 94, total N=223. **(C)** Representative pictures of hematoxylin-eosin (HE) stainings of control C4.1, mild P1.2, moderate P3.1 and severe P5.1 patient-derived organoids at day 20. **(D)** Representative images of control C3.1, mild P2.1, P3.2 and severe P5.1 patient-derived organoids stained for N-cadherin (N-CAD) at day 20. **(E)** Quantification of apical N-CAD signal in control, mild, moderate, and severe LIS1 patient-derived organoids at day 20, controls N=26, mild N=51, moderate N=46, severe N=86, total N=209. **(F)** Quantification of basal Ac-TUB strand density in DMSO and Epothilone D (EpoD, 1nM) treated control and LIS1-patient derived organoids at day 15, control DMSO N=22, control EpoD N=21, mild DMSO N=19, mild EpoD N=20, moderate DMSO N=14, moderate EpoD N=17, severe DMSO N= 30, severe EpoD N=31, total N=174. **(G)** VZ diameter quantification of DMSO and EpoD treated control- and LIS1 patient-derived organoids at day 15, control DMSO N=26, control EpoD N=39, mild DMSO N=28, mild EpoD N=23, moderate DMSO N=14, moderate EpoD N=15, severe DMSO N= 28, severe EpoD N=30, total N=203. **(H)** Representative DAPI pictures of control, mild, moderate and severe LIS1 patient-derived organoids treated with DMSO or EpoD. The yellow lines indicate the edges of the VZ areas, the red lines those of the cortical plate regions. Scale bars, (A left panel, H) 200 μ m, (A right panel, C, D) 20 μ m. Error bars, \pm SD. *P< 0.05, **P< 0.01, ***P< 0.001.

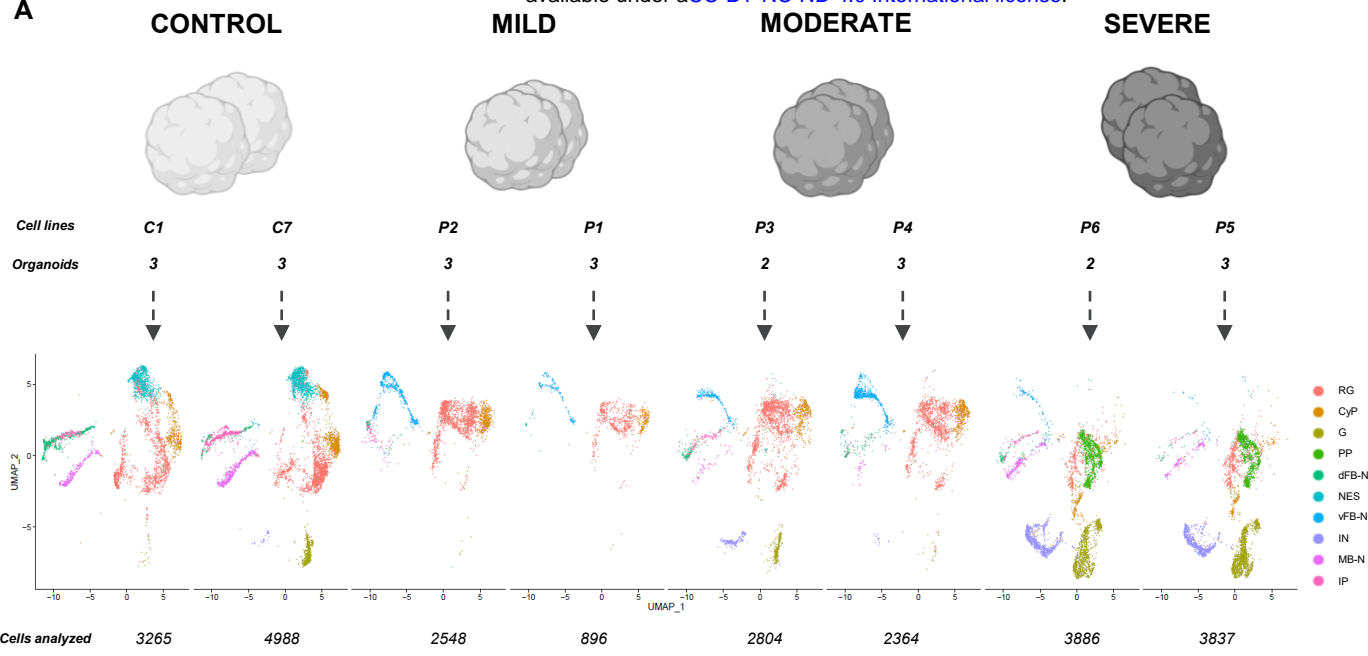
Figure 4: Disturbance in niche-dependent WNT-signaling is LIS1 severity-dependent.

(A) Representative images of WNT-GFP reporter control C3.1, mild P1.1, moderate 3.1 and severe P5.1 patient-derived organoids at day 20. **(B)** Quantification of mean value of WNT-GFP signal in VZ structures, control N=20, mild N=20, moderate N=10, severe N=10, total N=60. **(C)** Heatmap showing the expression of genes belonging to WNT signaling pathway in the CyP of each experimental group compared to control. **(D)** Representative magnifications of vertical, horizontal and oblique division planes in control (C4.1) and severe LIS1 (P5.1) patient-derived organoids and relative quantification of cell division plane orientation at day 20, control N=62, mild N=56, moderate N=44, severe N=56, total N=218. **(E)** Representative DAPI images of control 3.1, mild P1.1, moderate P4.2 and severe P6.1 LIS1 patient-derived organoids treated with DMSO or CHIR99021 (CHIR, 1 μ M). **(F)** VZ diameter quantification of DMSO and CHIR treated organoids, control DMSO N=27, control CHIR N=39, mild DMSO N=28, mild CHIR N=34, moderate DMSO N=24, moderate CHIR N=13, severe DMSO N= 28, severe CHIR N=38, total N=221. **(G)** Quantification of cell division plane

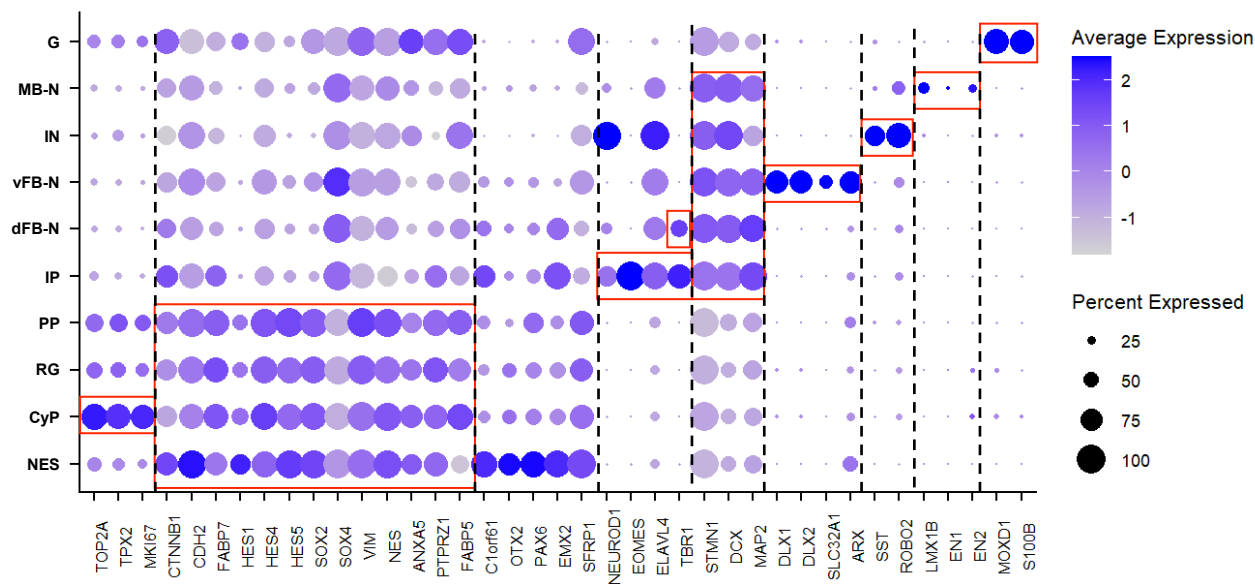
orientation in control and LIS1-patient derived organoids treated with DMSO or CHIR, control DMSO N=9, control CHIR N=9, mild DMSO N=9, mild CHIR N=9, moderate DMSO N=9, moderate CHIR N=9, severe DMSO N= 9, severe CHIR N=9, total N=72. (f) Scale bars (a) 50 μm , (c) 20 μm , (f) 200 μm . Error bars, $\pm\text{SD}$. *P< 0.05, **P< 0.01, ***P< 0.001.



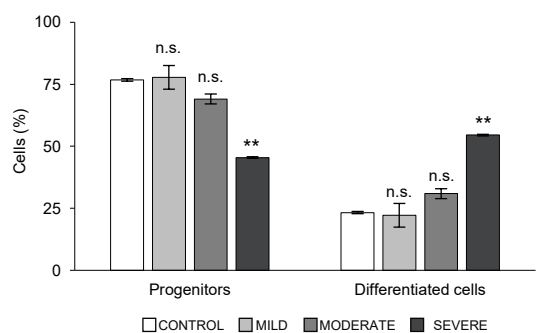
A



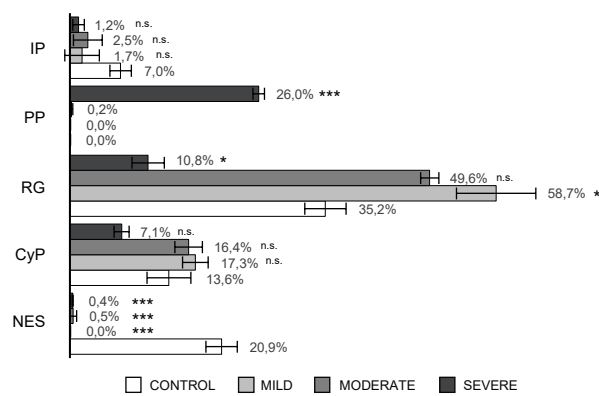
B



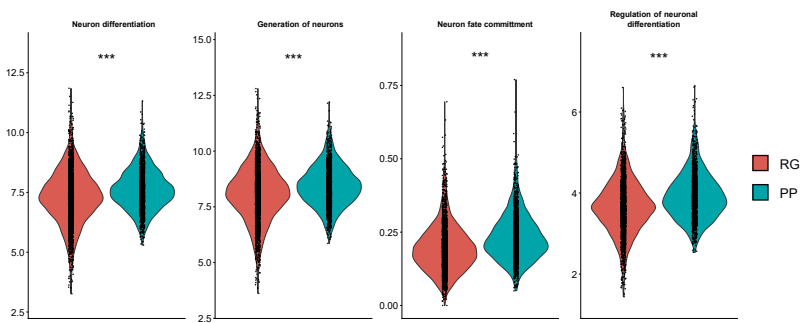
C



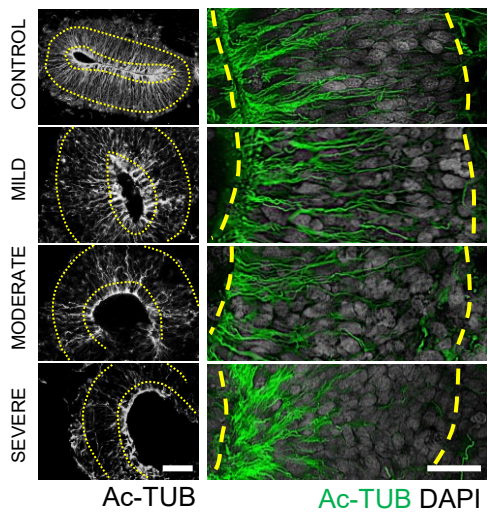
D



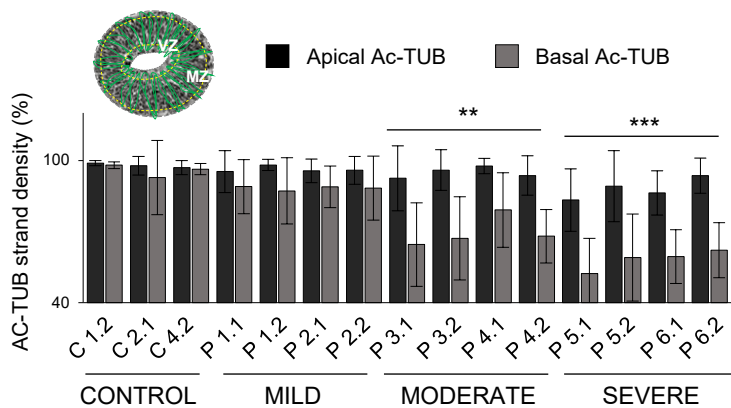
E



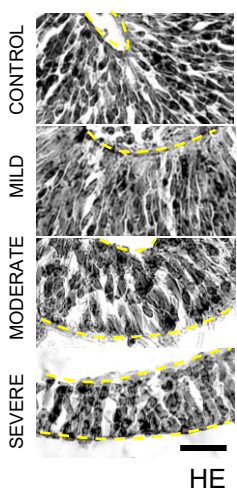
A



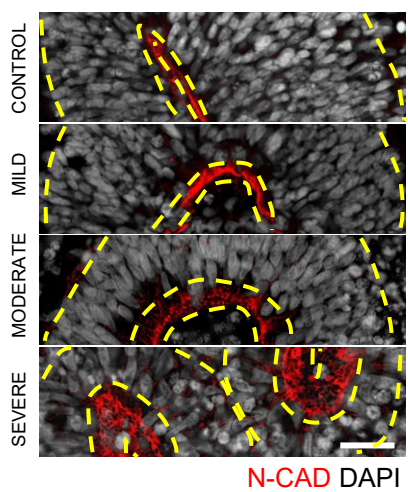
B



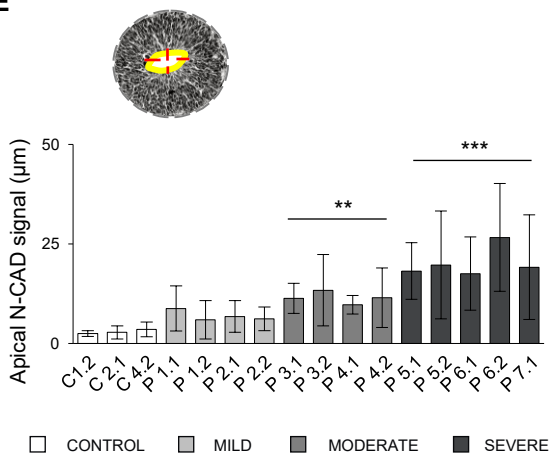
C



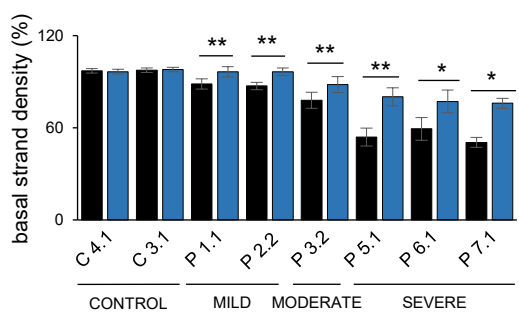
D



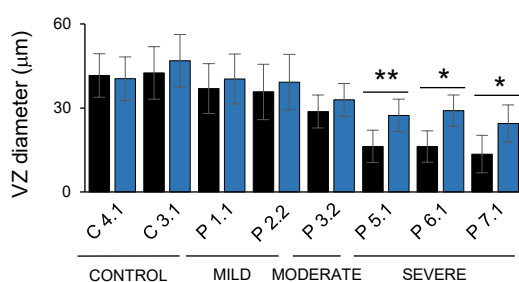
E



F

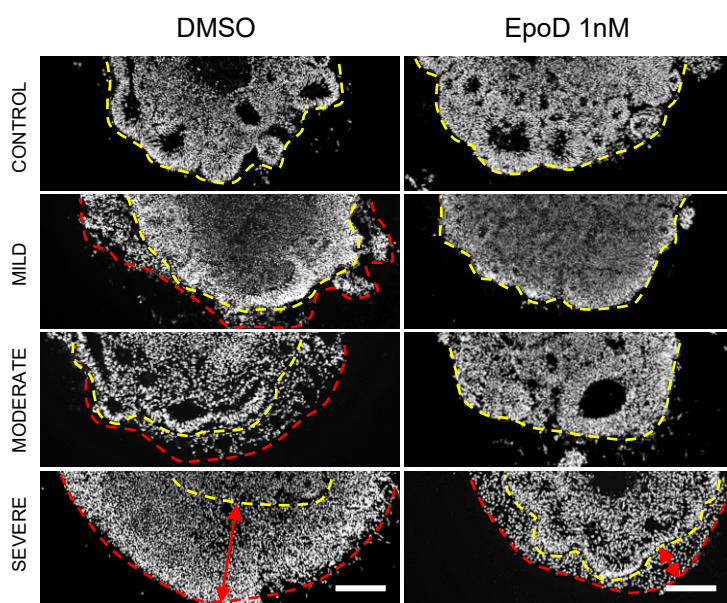


G



■ DMSO ■ EpoD

H



DAPI

